FUDMA Journal of Sciences (FJS)
ISSN online: 2616-1370
ISSN print: 2645 - 2944
Vol. 10 No. 21, November, 2026, pp 157 – 163
DOI: https://doi.org/10.33003/fjs-2026-1021-6171

Comparative XRD Characterization of Three SMAW Electrode Flux Coatings: Prospects for Nigerian Raw-Material Substitution

***Wilfred Onoshiorena Ikalumhe and Jeremiah Odion Akhimien**

Department of Mechanical Engineering, Edo State University, Iyamho, Edo State, Nigeria.

*Corresponding author e-mail: ikalumhe.wilfred@edouniversity.edu.ng

Received: 07 Oct. 2026
Accepted: 26 Oct. 2026
Published: 30 Oct. 2026

ABSTRACT

X-ray diffraction (XRD) was used to screen the crystalline phases in the flux coatings of three commercial shielded metal arc welding (SMAW) electrodes: a general-purpose rutile electrode (E6013), a cast-iron repair electrode (ENi-CI) and an austenitic stainless-steel electrode (E308-16). The aim was to produce a preliminary reference for later evaluation of locally sourced Nigerian raw materials. Coatings were removed by scraping, ground and sieved below 75 µm. Patterns were recorded on a Shimadzu XRD-6000 with Cu-Kα radiation (λ = 1.5406 Å) over 10–80° 2θ at a step size of 0.02°. Phases were identified provisionally by comparing peak positions with reference values. The E6013 coating showed reflections at 24.9°, 26.9° and 29.4°, provisionally matched to kaolinite (002), quartz (101) and calcite (104), plus an unresolved reflection at 31.8°. The strongest reflection of the cast-iron electrode coating, at 48.1°, is consistent with anatase TiO_2 (200). Its intensity relative to the absent anatase (101) reflection may indicate preferred orientation, but this could not be confirmed. The stainless-steel coating gave reflections consistent with γ-austenite (43.7°, 51.1°, 74.7°), together with a tentative reflection at 65.6° near the ferrite (200) position. These metallic reflections may arise wholly or partly from core-wire or metal-powder material in the scraped coating. Kaolinite and quartz reflections at 24.9° and 26.9° appeared in both the E6013 and stainless-steel coatings. The results are qualitative. No Rietveld refinement or phase quantification was performed, and neither local raw materials nor welding performance were tested. The data therefore offer a preliminary, phase-level reference for future evaluation of local kaolin, silica (including rice-husk-ash silica) and limestone, not evidence that substitution is feasible.

Keywords: X-ray Diffraction, Shielded Metal Arc Welding, Electrode Flux Coating, Phase Identification, Austenite, Delta-Ferrite; Locally Sourced Raw Materials

INTRODUCTION

Shielded metal arc welding (SMAW) remains one of the most widely used joining processes in fabrication, repair and maintenance welding largely because of its portability, versatility and low equipment cost. The performance of a SMAW consumable depends on the combined behaviour of its core wire and its flux coating. The coating typically constitutes 20–40 wt% of the electrode and is formulated from mineral powders, ferro-alloys and metal powders, organic constituents such as cellulose, and an alkali-silicate binder (Bajić et al., 2020). The coating performs three principal metallurgical functions: formation of a protective slag over the solidifying weld pool, stabilisation of the welding arc, and alloying or deoxidation of the weld metal (Gupta et al., 2023; Jastrzębska et al., 2015). Commonly reported mineral sources for these functions include rutile (TiO_2) and ilmenite ($FeTiO_3$) as arc stabilisers and slag formers, calcite ($CaCO_3$) and fluorspar (CaF_2) as slag-forming and shielding-gas-generating agents in basic and lime-titania coatings, silica (SiO_2) and clay minerals such as kaolin as binders and viscosity modifiers, and iron-oxide-rich additions such as red ochre or mill scale as iron-replenishing agents (Khan & Chhibber, 2021). Because the in-service behaviour of a flux coating – its slag detachability, arc stability, bead profile and contribution to weld-metal chemistry – is influenced by the crystalline phases present, together with bulk chemistry, amorphous binder content, particle size and processing rather than by the bulk elemental composition alone (Paniagua-Mercado & Lopez-Hirata, 2011), X-ray diffraction (XRD) is the principal non-destructive technique for resolving the mineralogical assemblage of a flux powder. Each crystalline phase gives rise to a unique set of diffraction maxima whose angular positions (2θ) are related to the interplanar spacings (d) of the constituent lattice planes through Bragg's law, $n\lambda = 2d\sin\theta$, so that observed $2\theta/d$ values can be compared directly with reference powder-diffraction data for candidate mineral and metallic phases (Surdu & Győrgy, 2023).

In Nigeria, the welding consumables market has been reported to depend substantially on imported electrodes and flux raw materials (Adeyeye, 2021), although the country has deposits of clay minerals, silica sand and limestone, and generates iron-oxide-bearing process residues, that are mineralogically comparable to several imported flux constituents. Ugoamadi (2010) reported that locally sourced raw materials could be formulated into manual metal-arc electrode coatings that performed competitively with imported, titania-based electrodes in terms of weld-metal tensile properties. Mineralogical studies of technical kaolin have reported kaolinite as the dominant phase, with accessory quartz and feldspar and SiO_2/Al_2O_3 ratios suited to ceramic and filler applications (Jibrin et al., 2024). Agro-industrial residues have also been explored as flux and filler sources – for example, calcined coconut-shell ash in welding-flux powders (Afolalu et al., 2020) and rice husk ash as a source of high-purity silica (Omatola et al., 2023).

Previous characterisation of SMAW and related fluxes has, however, concentrated largely on bulk chemistry and its effect on weld-metal composition (Khan & Chhibber, 2021), on the

thermophysical and physicochemical properties of designed flux systems (Gupta et al., 2023), or on the properties of the resulting slags (Jastrzębska et al., 2015), while local-sourcing studies have mainly reported elemental compositions or the mechanical performance of the welds produced (Ugoamadi, 2010; Adeyeye, 2021). Phase-resolved XRD data for the unfused coatings of commercially available electrodes remain scarce, particularly in a form that allows direct comparison with candidate local raw materials. In the absence of such reference data, it is difficult to determine whether a local kaolin, silica or limestone provides the same mineral phase as the imported constituent it is meant to replace, or merely a comparable oxide content. Characterizing the phases present in existing, commercially proven electrode coatings is therefore a sensible first step towards benchmarking local raw materials.

Flux and slag chemistry are also pertinent to arc-based additive manufacturing processes such as wire-arc additive manufacturing (WAAM), which relies on welding wires and arc sources closely related to those used in conventional joining (Srivastava et al., 2023). Phase-identification data for flux constituents may thus be of some relevance in that context, although WAAM predominantly uses solid wires and lies outside the scope of the present work.

This study aimed to establish a phase-resolved XRD benchmark for the flux coatings of three commercially representative SMAW electrodes – a general-purpose rutile/lime-titania electrode, a cast-iron repair electrode and an austenitic stainless-steel electrode – against which locally sourced Nigerian kaolin, silica, limestone and iron-oxide-bearing materials can subsequently be evaluated for flux reformulation. To this end, the crystalline phases in each coating were identified, and their characteristic peak positions, interplanar spacings and relative intensities were tabulated.

MATERIALS AND METHODS

Materials

Three commercial shielded metal arc welding (SMAW) electrodes, representative of the principal coating families encountered in general fabrication and repair welding, were examined: (i) a normal, general-purpose rutile/lime-titania-type electrode, Everstar Plus E6013 (AWS A5.1 classification), manufactured by Everstar Metal and Welding Materials Manufacturing Limited, with a specified tensile strength of 420 MPa, a yield strength of 330 MPa and a recommended welding current range of 50–90 A (Sample 1, “Normal Electrode”); (ii) a cast-iron repair electrode with a titania-rich coating formulation (Sample 2, “Cast Electrode”); and (iii) an austenitic stainless-steel electrode of the E308L/E316L family (Sample 3, “Stainless Steel Electrode”). For each electrode, the flux coating was carefully detached from the core wire by gentle mechanical scraping, taking care to avoid contamination from the metallic core, and the recovered material was ground in an agate mortar and sieved to a particle size below 75 µm to minimise preferred-orientation artefacts and ensure adequate particle statistics during data collection. Table 1 shows the properties of the various electrodes used.

Table 1: Specifications and Properties of the Three SMAW Electrodes Examined

Property	Sample 1: Normal Electrode	Sample 2: Cast Electrode [c]	Sample 3: Stainless Steel Electrode
General Information			
Manufacturer	Everstar Metal and Welding Materials Manufacturing Limited	Not identified	Dayang (DY Group Co. Ltd)
Brand / product	Everstar Plus E6013	Not identified	Dayang E308-16
AWS classification	AWS A5.1 E6013	AWS A5.15 ENi-CI	AWS A5.4 (ASME SFA-5.4) E308-16
Other standard	GB/T 5117-2012 E4313	EN ISO 1071 E C Ni-CI 1	—
Coating type	Rutile (high-titania)	Basic-graphite	Rutile (titania)
Diameter × length (mm)	2.5 (3/32") × 350	2.5 × 300	3.2 × 350
Polarity	AC / DC	DC (+)	AC / DC (+)
Welding current (A)	50–90	70–100	80–120
Net weight per pack	5 kg (11 lb)	5 kg (11 lb)	5 kg (11 lb)
Chemical Composition of Deposited Weld Metal (Wt%)			
C	≤ 0.12	≈ 0.5	≤ 0.08
Mn	0.30–0.60	—	0.5–2.5
Si	≤ 0.35	—	≤ 1.00
Cr	—	—	18.0–21.0
Ni	—	≥ 96	9.0–11.0
S	≤ 0.035	—	≤ 0.03
P	≤ 0.040	—	≤ 0.04
Mechanical Properties of Deposited Weld Metal			
Tensile strength, σb (MPa)	≥ 420	250	≥ 550 (typical 610)
Yield strength, σs (MPa)	≥ 330	200	Not specified
Elongation, δ5 (%)	≥ 17	3	≥ 35 (typical 43)
Impact energy, Akv (J)	≥ 47 at 0 °C	Not specifer	103 at 20 °C

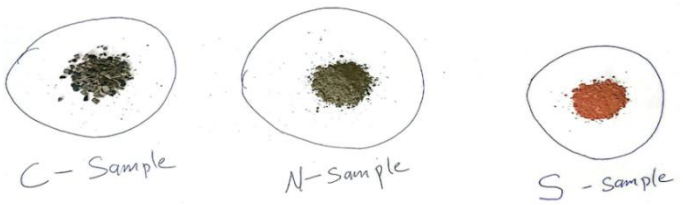


Plate 1: Detached Welding Electrode Flux from Samples C, N and S

XRD Data Acquisition

Powder XRD patterns were recorded on a Shimadzu XRD-6000 X-ray diffractometer operating with Cu-Kα radiation (λ = 1.5406 Å, Kα1) at 40 kV and 30 mA in Bragg–Brentano (θ–2θ) reflection geometry. Each pattern was collected over a 2θ range of 10–80° with a step size of 0.02° at a continuous scan rate of 2°/min (equivalent to a counting time of 0.6 s per step), yielding 3501 data points per sample. The incident and diffracted beams were defined by a 1° divergence slit, a 1° scatter slit and a 0.3 mm receiving slit. The instrument was calibrated against a silicon standard before measurement. Each powdered sample was mounted on a flat glass sample holder and levelled flush with the holder surface to minimise specimen-displacement errors.

Exclusion of core-wire contamination. To exclude contamination from the metallic core wire, the flux coating was removed by gentle scraping without cutting into the core, and the recovered fragments were inspected visually before grinding; any particle showing metallic lustre was discarded. Residual core contamination was then checked in the diffraction patterns by examining the positions of the strongest reflections of the core-wire phases: α-Fe (110) at 2θ ≈ 44.7° and (200) at ≈ 65.0° for the carbon-steel and cast-iron electrodes, and γ-Fe (austenite) (111) at ≈ 43.6° and (200) at ≈ 50.7° for the stainless-steel electrode. Any weak Fe reflections were interpreted with caution, because ferroalloy and iron-powder additions are normal constituents of SMAW flux coatings and produce reflections at the same positions.

Data Processing and Phase Identification

The as-collected intensity data (counts) were first corrected for background and for the Cu-Kα2 contribution (Kα2 stripping) using the Shimadzu data-processing software, and then smoothed using a Savitzky–Golay filter (21-point window, third-order polynomial) to attenuate counting-statistics noise while preserving peak positions and relative intensities (Figures 1–3). Peak positions (2θobs) were converted to interplanar spacings (dobs) using Bragg's law, d = λ/(2 sinθ). Candidate phases were identified by comparing dobs and 2θobs with literature/reference values reported for mineral phases common to welding-electrode flux systems (Jibrin et al., 2024; Khan & Chhibber, 2021; Omatola et al., 2023) and for austenite/ferrite phases in stainless steels. Where the deviation between observed and reference 2θ exceeded approximately 0.5° and no unambiguous match could be identified, the reflection is reported as tentative or unresolved, pending confirmation by Rietveld refinement against certified reference patterns.

Bragg's law $n\lambda = 2d \sin\theta$ equation (1)

Where n = order of diffraction

λ = X-ray wavelength (Cu-Kα = 1.5406 Å)

d = interplanar spacing between crystal planes

θ = Brags angle

while rearranging for d spacing:

$d = n\lambda/(2 \sin\theta)$ equation (2)

RESULTS AND DISCUSSION

Figures 1–3 present the powder XRD patterns recorded for the normal, cast and stainless-steel electrode flux coatings, respectively, over the 2θ range of 10–80°. The thin trace in each figure is the as-collected (raw) intensity, and the bold trace is the Savitzky–Golay-smoothed profile used for peak-position determination. Table 1 (Section 3.4) summarises the diffraction peaks identified in each pattern, together with their interplanar spacings, intensities and tentative phase assignments.

XRD Pattern of the Normal Electrode (Sample 1)

The diffraction pattern of the normal electrode (Figure 1) exhibits a relatively flat, low background of 2–4 counts across the measured range, indicating reasonable sample preparation and low fluorescence/incoherent scattering contributions. Superimposed on this background are a cluster of reflections in the 24–32° range, the most intense of which occur at 2θ = 29.4° (17 counts) and 31.8° (14 counts), with additional moderate reflections at 24.9° and 26.9°.

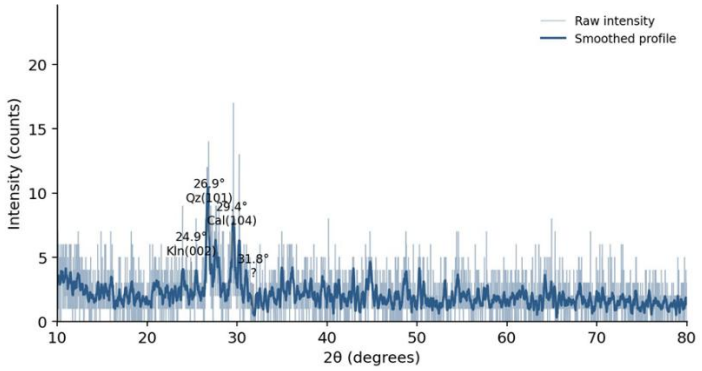


Figure 1: X-ray Diffraction Pattern of the Normal Electrode (Sample 1) Flux Coating. Thin Line: Raw Intensity; Bold Line: Savitzky–Golay-Smoothed Profile (21-Point Window, Third-Order Polynomial)

The reflection at 2θ = 29.4° (*d* = 3.036 Å) corresponds almost exactly to the (104) reflection of calcite ($CaCO_3$), for which the reference position is 2θ = 29.41° (Δ2θ = −0.01°). Calcite/limestone is a standard slag-forming and CO_2-generating shielding constituent in basic and lime-titania coating systems (Khan & Chhibber, 2021), and its presence as the most intense phase in the normal-electrode coating is consistent with this role. The reflection at 26.9° (*d* = 3.312 Å) is close to the (101) reflection of quartz (reference 2θ = 26.67°, Δ = +0.23°); silica is incorporated both as a discrete filler and as an intrinsic component of clay-based binders (Khan & Chhibber, 2021; Omatola et al., 2023). The reflection at 24.9° (*d* = 3.573 Å) is consistent with the second-order basal (002) reflection of kaolinite – obtained from a basal spacing *d*(001) ≈ 7.15 Å, giving a reference 2θ(002) ≈ 24.86° (Δ = +0.04°) – in agreement with the basal reflections reported for Nigerian kaolin clays (Jibrin et al., 2024), which are commonly employed as slip/binder agents in rutile and lime-titania coatings.

The remaining intense reflection at 31.8° (*d* = 2.812 Å) does not correspond closely to calcite, quartz or kaolinite and is not unambiguously assigned. It is tentatively attributed to a minor feldspar-group aluminosilicate phase, which is frequently reported as an accessory mineral in clay-based binder systems; a firm assignment would require Rietveld refinement against certified reference patterns. Overall, the normal-electrode pattern is consistent with a clay–silica–carbonate flux base (kaolinite + quartz + calcite, with a minor aluminosilicate accessory phase), in agreement with the general composition reported for rutile/lime-titania SMAW coatings (Khan & Chhibber, 2021).

XRD Pattern of the Cast Electrode (Sample 2)

The cast-electrode pattern (Figure 2) is markedly different from that of the normal electrode. Its dominant feature is an intense, well-resolved reflection at 2θ = 48.1° (11 counts; *d* = 1.890 Å), accompanied by weaker reflections at 27.1° and 28.9° (6–9 counts) and at 55.6° and 61.3° (6–9 counts).

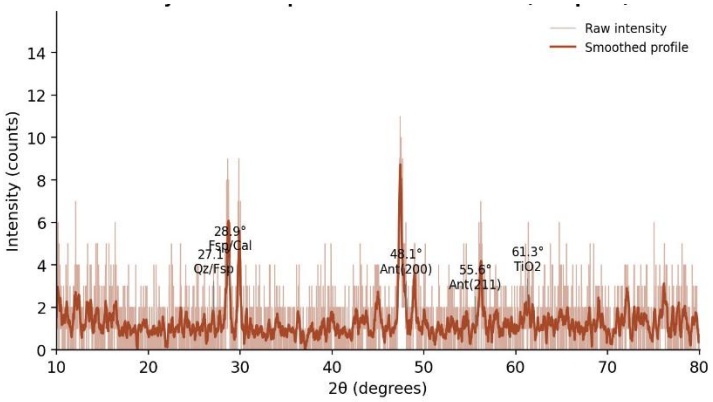


Figure 2: X-ray Diffraction Pattern of the Cast Electrode (Sample 2) Flux Coating. Thin Line: Raw Intensity; Bold Line: Savitzky–Golay-Smoothed Profile

The reflection at 48.1° corresponds remarkably closely to the (200) reflection of anatase TiO_2 (*a* = 3.785 Å), for which the calculated reference position is 2θ = 48.06° (Δ = +0.04°) (Thamaphat et al., 2008). Anatase is one of the two principal TiO_2 polymorphs supplied by rutile/ilmenite concentrates used as deoxidisers and arc stabilisers in welding-electrode coatings (Khan & Chhibber, 2021). Notably, the (101) reflection of anatase – normally its strongest by a wide margin, at a reference 2θ ≈ 25.3° – is comparatively weak or absent in this pattern. The dominance of the (200) reflection over the normally dominant (101) reflection is indicative of a pronounced preferred crystallographic orientation (texture) of the titania phase in this coating, which may arise from the platy or acicular morphology of the titania concentrate used, from the mechanical processing of the coating mix, or from a textured deposition of the powder during specimen preparation.

The pair of moderate-intensity reflections at 27.1° (*d* = 3.288 Å) and 28.9° (*d* = 3.087 Å) fall within the same 26–30° envelope occupied by the quartz/feldspar and calcite reflections identified in the normal electrode (Section 3.1), suggesting a broadly similar silicate/carbonate filler base across the two coating types. The weaker reflections at 55.6° (*d* = 1.652 Å) and 61.3° (*d* = 1.511 Å) are tentatively attributed to additional anatase contributions – the (211) reflection of anatase has a reference position of 2θ ≈ 55.10° (Δ = +0.50° for the 55.6° peak) – and to other TiO_2-polymorph or accessory-mineral reflections that remain unresolved at the present signal-to-noise level. Taken together, the cast-electrode pattern is consistent with a titania-rich (rutile/ilmenite-derived), texture-bearing coating formulation, a composition typically specified for cast-iron repair electrodes to promote arc stability, weld-pool fluidity and slag detachability on grey and ductile cast-iron substrates (Khan & Chhibber, 2021).

Since Sample 2 is a basic-graphite electrode with a pure-nickel core, nickel, graphite, calcite and fluorite were also considered as sources of the 48.1° reflection, but none was retained, because nickel (200) at 51.85° and graphite (102) at 50.7° lie more than 2° away, and although calcite (116) at 48.51° and fluorite (220) at 47.01° are closer, their much stronger (104) and (111) reflections, expected near 29.4° and 28.3°, are only weak in this pattern.

XRD Pattern of the Stainless Steel Electrode (Sample 3)

The stainless-steel electrode produced the most intense and the most structurally complex pattern of the three samples (Figure 3), with peak intensities reaching 20 counts and a larger number of resolvable reflections across the 2θ range of 24–75°.

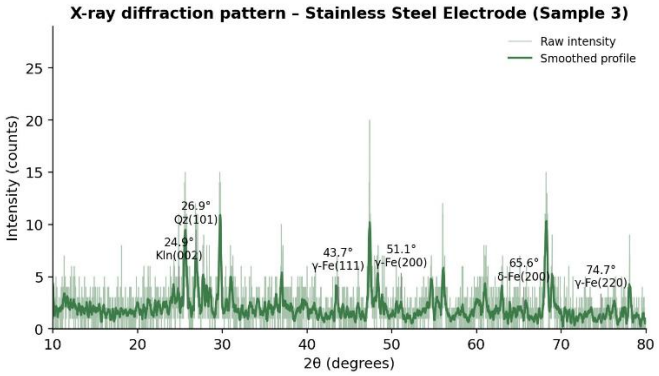


Figure 3: X-ray Diffraction Pattern of the Stainless Steel Electrode (Sample 3). Thin Line: Raw Intensity; Bold Line: Savitzky–Golay-Smoothed Profile

The three most intense reflections, at 2θ = 43.7° (20 counts, the overall maximum), 51.1° and 74.7°, correspond closely to the (111), (200) and (220) reflections of face-centred-cubic (FCC) γ-austenite (Fe–Cr–Ni solid solution, $a \approx 3.595$ Å), with reference positions of 43.57° (Δ = +0.13°), 50.75° (Δ = +0.35°) and 74.61° (Δ = +0.09°), respectively. This is consistent with the austenitic matrix expected of an E308L/E316L-type stainless-steel consumable. An additional reflection at 65.6° (d = 1.422 Å) corresponds closely to the (200) reflection of body-centred-cubic (BCC) δ-ferrite/α-Fe ($a \approx 2.866$ Å; reference 2θ = 65.03°, Δ = +0.57°). The coexistence of a minor BCC δ-ferrite fraction with the dominant FCC austenite is metallurgically expected, and indeed desirable, in austenitic stainless-steel weld deposits: a controlled δ-ferrite content suppresses solidification (hot) cracking during weld-metal cooling without significantly compromising corrosion resistance (Shin & Chun, 2024).

Significantly, the reflections at 24.9° and 26.9° – assigned in Section 3.1 to kaolinite (002) and quartz (101), respectively – recur in the stainless-steel pattern at essentially the same positions (Δ = +0.04° and +0.23°). Because these positions are inconsistent with any common FCC or BCC iron-based phase, they are attributable to residual clay/silica flux-coating constituents rather than to the metallic core or weld deposit. This indicates that, despite the very different core-wire metallurgy, the stainless-steel electrode shares a broadly similar clay–silica binder/filler base with the normal electrode, with the alloy-specific differentiation residing in the metallic core wire and any ferro-alloy additions rather than in the mineral filler system (Sham & Liu, 2014).

Comparative Analysis

Table 2: Collates the Diffraction Peaks Identified for all Three Samples, Together with their Interplanar Spacings, Intensities and Tentative Phase Assignments

Sample	$2\theta_{obs}$ (°)	d_{obs} (Å)	Intensity (counts)	Tentative phase assignment (hkl)	Reference 2θ (°), Δ
Normal Electrode (Sample 1)	24.9	3.573	Moderate	Kaolinite, (002)	24.86 (+0.04)
	26.9	3.312	Moderate	Quartz, (101)	26.67 (+0.23)
	29.4	3.036	17 (strongest)	Calcite, (104)	29.41 (−0.01)
	31.8	2.812	14	Unresolved aluminosilicate (feldspar-group)	—
Cast Electrode (Sample 2)	27.1	3.288	6–9	Quartz / feldspar, (101)/(002)	26.67–27.5 (≈0.0–0.4)
	28.9	3.087	6–9	Feldspar / carbonate residue	≈29.4 (≈−0.5)
	48.1	1.890	11 (dominant)	Anatase TiO_2, (200)	48.06 (+0.04)
	55.6	1.652	6–9	Anatase TiO_2, (211)	55.10 (+0.50)
	61.3	1.511	6–9	TiO_2 polymorph (unresolved)	—
Stainless Steel Electrode (Sample 3)	24.9	3.573	9–20	Kaolinite, (002) – flux residue	24.86 (+0.04)
	26.9	3.312	9–20	Quartz, (101) – flux residue	26.67 (+0.23)
	43.7	2.070	20 (highest)	γ-Austenite (FCC), (111)	43.57 (+0.13)
	51.1	1.786	9–20	γ-Austenite (FCC), (200)	50.75 (+0.35)
	65.6	1.422	9–20	Tentative / unresolved (possibly BCC (200))	65.03 (+0.57)
	74.7	1.270	9–20	γ-Austenite (FCC), (220)	74.61 (+0.09)

Table 2. Summary of diffraction peaks, interplanar spacings and tentative phase assignments for the three SMAW electrode flux coatings. Reference 2θ values were calculated from Bragg's law. using λ(Cu-Kα) = 1.5406 Å and standard lattice parameters for the indicated phases (calcite (104) d = 3.035 Å; quartz (101) d = 3.343 Å; kaolinite (002) d ≈ 3.575 Å; anatase a = 3.785 Å, c = 9.514 Å; γ-austenite a = 3.595 Å, FCC; δ-ferrite a = 2.866 Å, BCC). $\Delta = 2\theta_{obs} - 2\theta_{reference}$.

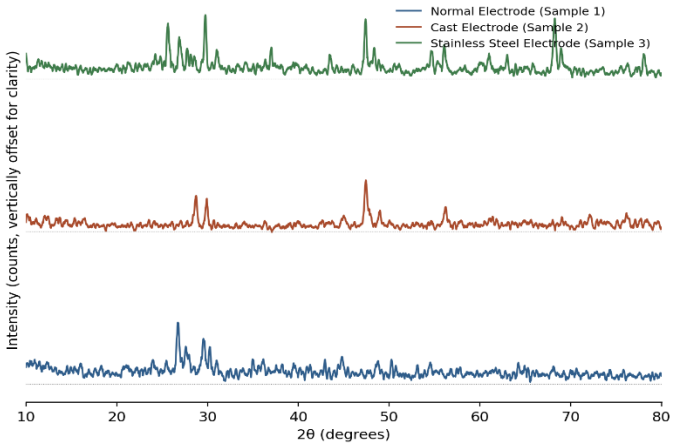


Figure 4: Comparative, Vertically Offset Overlay of the Savitzky–Golay-Smoothed XRD Patterns for the Normal, Cast and Stainless-Steel Electrode Flux Coatings

Three observations emerge from the comparative dataset. First, a kaolinite-(002)/quartz-(101) doublet near 2θ ≈ 24.9°/26.9° is common to the normal and stainless-steel electrodes, indicating that the same families of slip clays and silica fillers are used across electrode grades with very different core-wire chemistries; the alloying differentiation between electrode types therefore appears to reside primarily in the metallic core and any ferro-alloy/metal-powder additions, rather than in the clay/silica binder–filler base (Khan & Chhibber, 2021; Ugoamadi, 2010). Second, the cast electrode is mineralogically distinct, being dominated by a strongly textured anatase phase rather than by the calcite/quartz/kaolinite assemblage that characterises the normal electrode; this is consistent with a deliberately titania-rich formulation tailored for cast-iron repair welding. Third, only the stainless-steel electrode displays the metallic γ-austenite/δ-ferrite reflections, confirming the two-phase (predominantly austenitic, minor ferritic) microstructure expected of a stabilised austenitic stainless-steel consumable (Shin & Chun, 2024); these reflections are entirely absent from the normal and cast electrode patterns, as expected given their mild-steel core wires and the absence of comparable FCC/BCC iron-alloy reflections in the 40–80° range of those patterns.

Implications for Locally Sourced Raw Material Substitution

The phase-resolved benchmark established here provides specific, mineral-level targets against which candidate Nigerian raw materials can be evaluated for flux reformulation, complementing the purely-compositional (XRF/EDS-based) comparisons that have dominated previous local-sourcing studies. Kaolin deposits from several Nigerian states have been shown to contain kaolinite as the dominant phase, accompanied by quartz, feldspar and minor iron-oxide phases, with SiO_2/Al_2O_3 ratios and basal-reflection positions comparable to the kaolinite (002) reflection identified in the normal and stainless-steel electrode coatings (Obonyilo et al., 2026); such clays are therefore directly comparable, on a phase-matching basis, to the binder/filler clay identified in the present samples. Similarly, silica derived from rice husk ash and processed via thermal or sol–gel routes has been shown to yield predominantly crystalline silica phases (quartz/cristobalite) (Omatola et al., 2023), offering a renewable, agro-industrial substitute for the quartz (101) reflection observed at 26.9°/27.1° in all three electrode types. Widely available Nigerian limestone deposits represent an obvious domestic source for the calcite (104) phase that dominates the normal-electrode pattern, while iron-oxide-rich process residues such as mill scale from integrated steel plants have already been demonstrated as viable iron-replenishing flux constituents in locally formulated electrodes (Ugoamadi, 2010).

For the cast electrode, the identification of a strongly textured anatase phase as the dominant constituent suggests that locally available titania-bearing mineral sands (rutile/ilmenite concentrates), where accessible, would need to be evaluated not only for TiO_2 content but also for the particle morphology that gives rise to the observed (200)-dominant texture, since this texture may be linked to specific arc-stability or slag-detachability characteristics of the cast-electrode coating. In all cases, the present results indicate that future substitution studies should report XRD phase data – peak positions, d-spacings and relative intensities – for candidate local materials in the same format as Table 2, enabling direct, phase-by-phase comparison with the reference electrode coatings characterised here, in addition to the elemental (XRF/EDS) comparisons typically reported (Obonyilo et al., 2026; Omatola et al., 2023; Ugoamadi, 2010).

CONCLUSION

X-ray diffraction analysis of the flux coatings of three representative SMAW electrode types produced three distinct diffraction patterns, from which provisional phase matches were made on the basis of a limited number of observed reflections. The normal (rutile/lime-titania) electrode showed reflections provisionally matched to a clay–silica–carbonate assemblage: kaolinite (002) at 2θ = 24.9°, quartz (101) at 26.9°, calcite (104) at 29.4° (the strongest reflection), and an unresolved aluminosilicate phase at 31.8°. The cast electrode showed its strongest reflection at 48.1°, provisionally assigned to an anatase TiO2 (200) reflection (Δ = +0.04° from the reference position). The high intensity of this reflection relative to the normally strongest anatase (101) reflection may reflect preferred orientation of the titania phase, although this cannot be confirmed without whole-pattern fitting. Weaker reflections were also observed and provisionally matched to subsidiary silicate and additional titania-polymorph phases. The stainless-steel electrode showed reflections at 43.7°, 51.1° and 74.7° consistent with γ-austenite (111), (200) and (220), with an accompanying reflection at 65.6° consistent with δ-ferrite (200). Because these are metallic phases rather than typical flux minerals, they may originate wholly or partly from residual core-wire or metal-powder material in the

scraped coating, and they should not be interpreted as evidence of a weld-metal microstructure, which was not examined in this study. Residual kaolinite and quartz reflections at 24.9° and 26.9° suggest a flux base shared with the normal electrode.

These provisional phase identifications, together with their associated d-spacings and relative intensities (Table 2), provide a qualitative, preliminary reference that may inform the substitution of imported electrode-coating constituents with locally sourced Nigerian kaolin, rice-husk-ash-derived silica, limestone and iron-oxide-bearing process residues, but they do not by themselves show that such substitution is feasible. The findings are subject to three limitations. First, although care was taken to avoid the metallic core, contamination of the scraped coatings by core-wire material cannot be fully excluded, particularly for the stainless-steel electrode. Second, no Rietveld refinement or quantitative phase analysis was performed, so the assignments are qualitative and provisional, and no phase proportions are implied. Third, neither locally sourced raw materials nor the welding performance of the electrodes were tested. Future work should therefore begin with Rietveld refinement and quantitative phase analysis, using longer counting times, to confirm the tentative assignments made here, particularly for the unresolved reflections at 31.8° and 61.3°. These diffraction results should then be cross-checked against complementary XRF/EDS and FTIR data on the same samples, in line with ongoing characterisation work on locally sourced electrode flux materials. Once the assignments are confirmed, the same phase-matching approach can be extended to candidate Nigerian raw materials, and electrodes reformulated with these materials should be tested for welding performance before any substitution is recommended.

REFERENCES

Adeyeye, A. D. (2021). Current trends in welding flux development. *Nigerian Journal of Technology, 40*(2), 241–251.

Afolalu, S. A., Samuel, O. D., & Ikumapayi, O. M. (2020). Development and characterization of nano-flux welding powder from calcined coconut shell ash admixture with FeO particles. *Journal of Materials Research and Technology, 9*(4), 9232–9241. https://doi.org/10.1016/j.jmrt.2020.06.067

Bajić, D., Mrdak, M., Bajić, N., Veljić, D., Rakin, M., & Radosavljević, Z. (2020). Development of coated electrodes with solid wire and flux-cored alloyed wire for microalloyed steel welding. *Materials, 13*(9), Article 2152. https://doi.org/10.3390/ma13092152

Jibrin, A. I., Dalorima, U. L., Salihu, B., Mohammed, H., & Maigari, A. S. (2024). *Assessment of Industrial Potential of Kaolinite Clays from Bauchi, Ne Nigeria*. https://doi.org/10.60692/e30z5-3y489

Gupta, A., Singh, J., & Chhibber, R. (2023). Investigation of thermophysical and physicochemical characteristics of Al_2O_3-SiO_2-CaO-Na_3AlF_6 flux for SMAW electrode coating. *Silicon, 15*(8), 3463–3477.

Jastrzębska, I., Szczerba, J., Stoch, P., Prorok, R., & Śnieżek, E. (2015). Effect of electrode coating type on the physico-chemical properties of slag and welding technique. *Biuletyn Instytutu Spawalnictwa, 1*, Article 201537.

Khan, W. N., & Chhibber, R. (2021). Investigations on effect of CaO-CaF_2-TiO_2-SiO_2 based electrode coating constituents and their interactions on weld chemistry. *Ceramics International, 47*(9), 12483–12493. https://doi.org/10.1016/j.ceramint.2021.01.106

Omatola, K. M., Onojah, A. D., Amah, A. N., & Ahemen, I. (2023). Synthesis and characterization of silica xerogel and aerogel from rice husk ash and pulverized beach sand via sol-gel route. *Journal of the Nigerian Society of Physical Sciences, 5*(4), Article 1609. https://doi.org/10.46481/jnsps.2023.1609

Paniagua-Mercado, A. M., & Lopez-Hirata, V. M. (2011). Chemical and physical properties of fluxes for SAW of low-carbon steels. *Arc Weld, 13*, 281–298.

Sham, K., & Liu, S. (2014). Flux coating development for SMAW consumable electrode of high nickel alloys. *Welding Journal, 93*(8), 271s–281s.

Shin, M.-C., & Chun, E.-J. (2024). Effect of δ-ferrite formation and self-tempering behavior on mechanical properties of type 410 martensitic stainless steel fabricated via laser powder bed fusion. *Materials, 17(22), Article 5614*. https://doi.org/10.3390/ma17225614

Srivastava, M., Rathee, S., Tiwari, A., & Dongre, M. (2023). Wire arc additive manufacturing of metals: A review on processes, materials and their behaviour. *Materials Chemistry and Physics, 294*, Article 126988. https://doi.org/10.1016/j.matchemphys.2022.126988

Surdu, V.-A., & Győrgy, R. (2023). X-ray diffraction data analysis by machine learning methods—A review. *Applied Sciences, 13*(17), Article 9992. https://doi.org/10.3390/app13179992

Thamaphat, K., Limsuwan, P., & Ngotawornchai, B. (2008). Phase characterization of TiO_2 powder by XRD and TEM. *Agriculture and Natural Resources, 42*(5), 357–361.

Ugoamadi, C. C. (2010). Production of manual metal arc welding electrodes with local raw materials. *Nigerian Journal of Technology, 29*(1), 121–125.

Obonyilo, O. S., & Agu, M. N. (2026). Assessment of kaolin deposits in ogbadibo and otukpo local government areas of benue state using nuclear analytical technique and their possible applications in industry. *Fudma journal of sciences, 10*(5), 66-72.

©2026 This is an Open Access article distributed under the terms of the Creative Commons Attribution 4.0 International license viewed via https://creativecommons.org/licenses/by/4.0/ which permits unrestricted use, distribution, and reproduction in any medium, provided the original work is cited appropriately.